

# Hybridization of Multiple Vibrational Modes via Strong Coupling Using Confined Light Fields

Kishan S. Menghrajani,\* Henry A. Fernandez, Geoffrey R. Nash, and William L. Barnes\*

**Strong coupling of molecules placed in an optical microcavity may lead to the formation of hybrid states called polaritons, states that inherit characteristics of both the optical cavity modes and the molecular resonance. This is possible for both excitonic and vibrational molecular resonances. Previous work has shown that strong coupling may be used to hybridize two different excitonic resonances; this can be achieved when more than one molecular species is included in the cavity. Here it is shown that under suitable conditions three different molecular vibrational resonances of the same molecular unit may also be coupled together, the resulting polariton having characteristics of all three vibrational resonances. These results suggest that strong coupling might be used to manipulate vibrational resonances in a richer and subtler way than previously considered, opening a path to greater control of molecular systems and molecular processes via vibrational strong coupling.**

## 1. Introduction

Placing ensembles of molecules that possess an optically active transition inside a confined light field such as an optical microcavity may lead to a phenomenon known as strong coupling, in which new hybrid states called polaritons are created that are part molecule, part light.<sup>[1,2]</sup> Strong coupling is attracting increasing attention, in part because of exciting prospects for modifying chemistry.<sup>[3–8]</sup> There are two key features associated with this kind of strong coupling that underlie the recent surge of interest. First, strong coupling may change molecular energy levels leading, for example, to modified chemical landscapes,<sup>[9,10]</sup> and control over photochemistry.<sup>[11]</sup> Second, strong coupling results in coherent coupling of the molecules, with prospects, for example, of changing exciton transport.<sup>[12]</sup> In addition, strong coupling can be used to modify the transfer of energy between two species of molecule in a cavity, both where the species are intermixed<sup>[13–15]</sup> and where the two species are spatially separated.<sup>[15,16]</sup> In the visible regime a potentially more radical step is to use strong coupling

to hybridize excitonic resonances associated with two different species.<sup>[17,18,15]</sup> Hybridization of different vibrational overtones of an excitonic resonance of a single molecular species has also been achieved.<sup>[19,20]</sup> Meanwhile, in the infrared regime, hybridization of vibrational resonances associated with two distinct molecular species has also been reported recently.<sup>[21,22]</sup> While hybridization of two different vibrational resonances of a single molecular species to a cavity mode were reported by George et al.<sup>[23]</sup> Here we present results of experiments that show hybridization of three vibrational resonances of a single mode species to first a cavity mode and second a surface plasmon mode, thereby adding a potentially important component in the strong coupling toolbox, one that may further the degree of control possible over molecular vibrational states in any future polaritonic chemistry.


Strong coupling of vibrational modes was first explored using a planar cavity filled with the polymer polymethyl-methacrylate (PMMA) where the cavity mode was strongly coupled to the C=O vibrational resonance in the polymeric material.<sup>[24,25]</sup> Several further investigations have since been reported,<sup>[26–33]</sup> involving vibrational resonances in liquids,<sup>[34]</sup> transition metal complexes,<sup>[33]</sup> and liquid crystals.<sup>[35]</sup> Strong coupling of vibrational resonances has also been reported to help catalyze and inhibit chemical reactions<sup>[36]</sup> and to control the nonlinear optical response in the infrared.<sup>[37]</sup> 2D spectroscopy of molecular vibrations in an optical microcavity has also been explored.<sup>[38,39]</sup>

In the present work, we make use of two different types of confined light field. First we use the well-established planar optical microcavity, second we make use of the surface plasmon mode associated with a single metal surface. Surface plasmons on planar metal films have momenta that cannot be accessed easily by incident light; therefore, we employ grating coupling to overcome this problem, an approach previously explored for strong coupling of excitonic resonances.<sup>[40,41]</sup> In what follows, we briefly describe the sample structure and material properties. The main probe we use to explore the coupling between vibrational resonances and the optical modes of our confined light fields is to determine the dispersion of the polaritons involved. We describe how these data are acquired and present results from both types of cavity. We then discuss the modeling we have undertaken, both numerical and analytical, before summarizing our findings.

## 2. Results and Discussion

Schematics of the structures we used are shown in **Figure 1**. The optical microcavity was based on two gold mirrors 12 nm

K. S. Menghrajani, H. A. Fernandez, Prof. G. R. Nash,  
Prof. W. L. Barnes  
College of Engineering, Mathematics and Physical Sciences  
University of Exeter  
Exeter EX4 4QF, UK  
E-mail: km508@exeter.ac.uk; w.l.barnes@exeter.ac.uk

 The ORCID identification number(s) for the author(s) of this article can be found under <https://doi.org/10.1002/adom.201900403>.

© 2019 The Authors. Published by WILEY-VCH Verlag GmbH & Co. KGaA, Weinheim. This is an open access article under the terms of the Creative Commons Attribution License, which permits use, distribution and reproduction in any medium, provided the original work is properly cited.

The copyright line was changed on 13 September 2019 after initial publication.

DOI: 10.1002/adom.201900403

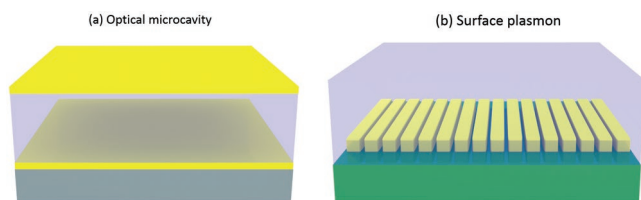


**Figure 1.** Schematics of the confined light field structures. a) An optical microcavity formed of two gold mirrors separated by a cavity-filling layer of the polymer PMMA, the substrate is a silicon wafer. b) A 1D metal grating supporting a surface plasmon mode, on top of a CaF<sub>2</sub> substrate, and overlain by a layer of PMMA.

thick, the space between them being filled with PMMA so as to form a PMMA-filled planar microcavity. A thickness of 2.26 μm was chosen for the cavity to ensure that the lowest order cavity resonance was close to the molecular vibrational resonances of interest. Further fabrication details are given in the Experimental Section below.

We chose the polymer PMMA as our molecular material. A sample infrared transmittance spectrum, acquired at normal incidence using Fourier-transform infrared spectroscopy (FTIR), for a 1 μm film of PMMA on a silicon wafer substrate is shown in **Figure 2**. For comparison the numerically calculated normal incidence transmittance of the bare cavity mode is shown in red, while the normal incidence experimentally measured transmission of PMMA-filled cavity is shown as a blue dot-dashed curve. Further details of the FTIR measurements and numerical calculation approach are given in the Experimental Section below. Many absorption features are present in this spectrum, notably a strong absorption due to the C=O

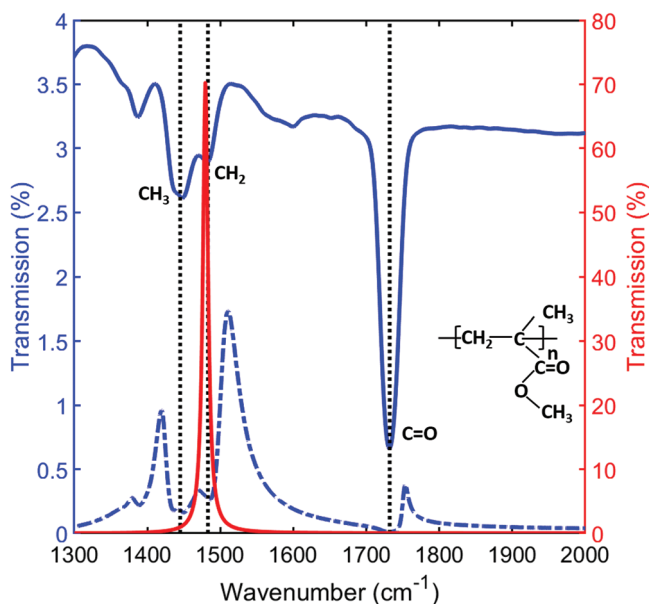


**Figure 2.** Normal incidence FTIR transmission spectra. The blue solid and dash-dotted curves show the measured transmittance of bare PMMA on a Si substrate and the measured transmittance of the cavity sample respectively. The red curve shows the numerically simulated transmittance of the bare cavity, as shown in Figure 1a, calculated by assuming the vibrational resonances to have zero strength. The dashed black lines represent C=O, CH<sub>2</sub>, and CH<sub>3</sub> vibrational modes.

stretching mode is clearly seen at 1732 cm<sup>-1</sup>.<sup>[42,43]</sup> The other features of interest in the present work are those that form the somewhat complex absorption band centered around 1445 cm<sup>-1</sup>, arising primarily from a bending resonance associated with -CH<sub>3</sub> together with a band centered around 1481 cm<sup>-1</sup>, arising primarily from a bending resonance associated with -CH<sub>2</sub>.<sup>[42,43]</sup> Hereafter we will refer to these as the C=O, CH<sub>3</sub>, and CH<sub>2</sub> resonances respectively. Although other resonance features are present, these three features capture the majority of the response so that, for simplicity, we concentrate on just these three resonances in this work. The C=O stretch has a measured Gaussian full width half-maximum (FWHM) of ≈30 cm<sup>-1</sup> whilst the CH<sub>2</sub> and CH<sub>3</sub> resonances both have a measured Gaussian FWHM of ≈60 cm<sup>-1</sup>.

To acquire dispersion plots we recorded FTIR spectra for a range of incident angles.

All measurements were performed with a spectral resolution of 4 cm<sup>-1</sup> and an angular resolution of 2°. An example of a measured dispersion diagram is presented in **Figure 3a**. Data were normalized with respect to a transmittance spectrum acquired with no sample present, and were recorded for positive angles only. They have been replicated at negative angles in Figure 3a for clarity.

The data in Figure 3a show a clear anticrossing at an angle of θ = 50°, indicative of strong coupling between the C=O (1732 cm<sup>-1</sup>) and the cavity mode. The strength of the splitting relative to the modal widths is discussed below. Indeed, coupling of the C=O, CH<sub>2</sub>, and CH<sub>3</sub> modes to the same cavity mode leads to the formation of four polariton bands: a lower polariton (L), a lower middle polariton (M1), an upper middle polariton (M2), and an upper polariton (U); these are shown as red, blue, green, and magenta dashed lines in Figure 3a respectively.

To gain greater insight into these data we undertook both numerical and analytical modeling. For the numerical modeling, we used a commercial finite-element package (details in Experimental Section below), while for analytical modeling we used a four coupled oscillator model. In the numerical modeling, we made use of a Drude model for the optical response of gold for the material parameters

$$\epsilon(\omega) = \epsilon_b - \frac{\omega_p^2}{\omega^2 + i\gamma\omega} \quad (1)$$

with parameters taken from Olmon et al.,<sup>[44]</sup> specifically, ω<sub>p</sub> = 1.29 × 10<sup>16</sup> rad s<sup>-1</sup>, and γ = 7.30 × 10<sup>13</sup> rad s<sup>-1</sup>, with ε<sub>b</sub> = 1.0. For the PMMA, we used a model based on three Lorentz oscillators

$$\epsilon(\omega) = \epsilon_\infty + \sum_j \frac{\omega_j^2 f_j}{\omega_j^2 - \omega^2 - i\gamma\omega} \quad (2)$$

with parameters given in **Table 1**, and with ε<sub>∞</sub> taken to be 1.99. The parameters for silicon in the infrared are based on data compiled by Edwards<sup>[45]</sup> and are taken to be, ε = 11.76 + 0.001i, while for air we took ε = 1.0. Finally, CaF<sub>2</sub> data were taken from Malitson,<sup>[46]</sup> at 5.0 μm the refractive index is n = 1.40; these data will be useful for the surface plasmon experiments discussed below.

Employing these parameters we used COMSOL to evaluate numerically the transmittance of the structure shown in

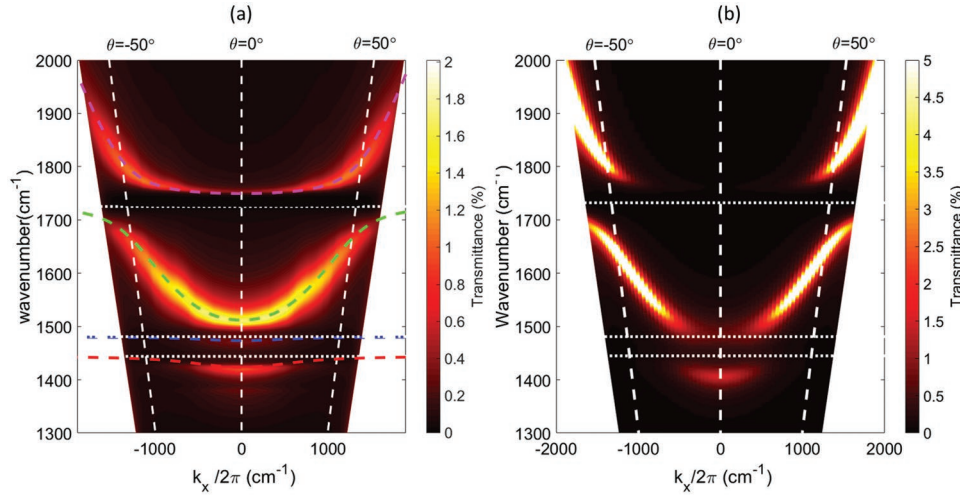


**Figure 3.** Dispersion plots for the cavity system. a) Experimental data. The measured infrared transmittance of the sample shown in Figure 1a is plotted as a function of frequency  $\text{cm}^{-1}$  and in-plane wavevector  $k_x$ . The horizontal white dotted lines indicate the energy of the C=O ( $1732 \text{ cm}^{-1}$ ),  $\text{CH}_2$  ( $1481 \text{ cm}^{-1}$ ), and  $\text{CH}_3$  ( $1445 \text{ cm}^{-1}$ ) vibrational resonances. The maximum polar angle for which these data were acquired was  $\Theta = 70^\circ$ . The angles of incidence equal to  $\pm 50^\circ$  are indicated as white dashed lines, and correspond to the angles at which anti-crossing of the cavity mode occurs with the C=O bond. Also shown are the calculated positions (colored dashed lines) of the polariton branches from the coupled oscillator model: lower polariton (red), lower middle polariton (blue), upper middle polariton (green), and upper polariton (magenta). b) Numerically modeled data using COMSOL Multiphysics. The calculated transmittance is shown as a function of frequency  $\text{cm}^{-1}$  and in-plane wavevector  $k_x$ .

Figure 1a as a function of frequency and in-plane wavevector; these data are shown in Figure 3b. We tested results from numerical modeling against those from a transfer matrix approach and found good agreement. We used the numerical approach here because it facilitated analysis of the grating structures we employed. The data show a good match to those acquired from experiment (shown in Figure 3a), giving us confidence that we have selected appropriate modeling parameters. The difference in absolute transmittance values between the experimental data (Figure 3a) and the modeled data (Figure 3b) is attributed to the slightly rough nature of the reverse side of the Si wafer substrate used in our experiments.

Next, for the analytical model, the four oscillators are the confined light field and the three vibrational modes, C=O,  $\text{CH}_2$ , and  $\text{CH}_3$ . The model can be captured by the following matrix equation

$$\begin{pmatrix} E_{\text{cl}} & \Omega_{\text{C=O}}/2 & \Omega_{\text{CH}_2}/2 & \Omega_{\text{CH}_3}/2 \\ \Omega_{\text{C=O}}/2 & E_{\text{C=O}} & 0 & 0 \\ \Omega_{\text{CH}_2}/2 & 0 & E_{\text{CH}_2} & 0 \\ \Omega_{\text{CH}_3}/2 & 0 & 0 & E_{\text{CH}_3} \end{pmatrix} \begin{pmatrix} a_{\text{L,M1,M2,U}} \\ b_{\text{L,M1,M2,U}} \\ c_{\text{L,M1,M2,U}} \\ d_{\text{L,M1,M2,U}} \end{pmatrix} = E_{\text{L,M1,M2,U}} \begin{pmatrix} a_{\text{L,M1,M2,U}} \\ b_{\text{L,M1,M2,U}} \\ c_{\text{L,M1,M2,U}} \\ d_{\text{L,M1,M2,U}} \end{pmatrix} \quad (3)$$

**Table 1.** Lorentz oscillator model parameters for the PMMA vibrational modes.

Vibrational mode	$f_j$	$\omega_j [\text{rad s}^{-1}]$	$\gamma_j [\text{rad s}^{-1}]$
C=O ( $j = 1$ )	0.0165	$3.26248 \times 10^{14}$	$5 \times 10^{12}$
$\text{CH}_2$ ( $j = 2$ )	0.0047	$2.7896 \times 10^{14}$	$9.3 \times 10^{12}$
$\text{CH}_3$ ( $j = 3$ )	0.0087	$2.72187 \times 10^{14}$	$12 \times 10^{12}$

where  $E_{\text{CL}}$  is the energy of the confined light field, i.e., the cavity/plasmon mode as appropriate, and is a function of the in-plane component of the wavevector,  $k_x$ .

$E_{\text{C=O}}$  is the energy of the C=O vibrational mode,  $E_{\text{CH}_2}$  is the energy of the  $\text{CH}_2$  vibrational mode and  $E_{\text{CH}_3}$  is the energy of the  $\text{CH}_3$  vibrational mode. The constants  $\Omega_{\text{C=O}}/2$ ,  $\Omega_{\text{CH}_2}/2$ , and  $\Omega_{\text{CH}_3}/2$  are the coupling strength of  $E_{\text{CL}}$  with  $E_{\text{C=O}}$ ,  $E_{\text{CH}_2}$ , and  $E_{\text{CH}_3}$ , respectively. The eigenvalues  $E_{\text{L,M1,M2,U}}$  of this matrix correspond to the lower (L), lower middle (M1), upper middle (M2), and upper (U) polariton bands. To fit these polariton bands to the measured dispersion, we set the three coupling strengths,  $\Omega_{\text{C=O}}$ ,  $\Omega_{\text{CH}_2}$ , and  $\Omega_{\text{CH}_3}$  as free parameters. The composition of the polariton bands are described by the generalized Hopfield coefficients  $|a_{\text{L,M1,M2,U}}|^2$ ,  $|b_{\text{L,M1,M2,U}}|^2$ ,  $|c_{\text{L,M1,M2,U}}|^2$ , and  $|d_{\text{L,M1,M2,U}}|^2$  where  $|a_{\text{L,M1,M2,U}}|^2 + |b_{\text{L,M1,M2,U}}|^2 + |c_{\text{L,M1,M2,U}}|^2 + |d_{\text{L,M1,M2,U}}|^2 = 1$ . The polariton bands can be written as  $|a_{\text{L,M1,M2,U}}|^2 |E_{\text{CL}} + |d_{\text{L,M1,M2,U}}|^2 |E_{\text{C=O}} + |b_{\text{L,M1,M2,U}}|^2 |E_{\text{CH}_2} + |c_{\text{L,M1,M2,U}}|^2 |E_{\text{CH}_3}$ , so that the Hopfield coefficients measure the extent to which the cavity mode, the C=O mode, the  $\text{CH}_2$ , and the  $\text{CH}_3$  modes contribute to each polariton band. Data for the bare microcavity  $E_{\text{cav}}$  and bare plasmon modes  $E_{\text{plas}}$  were obtained from modeling a PMMA-filled microcavity with the oscillator strength of the vibrational modes set to zero (see Figures S2 and S4 in the Supporting Information respectively).

We found that the best fit to our cavity data was obtained with:  $\Omega_{\text{C=O}} = 150 \text{ cm}^{-1}$ ,  $\Omega_{\text{CH}_2} = 40 \text{ cm}^{-1}$ , and  $\Omega_{\text{CH}_3} = 70 \text{ cm}^{-1}$  these values agree well with those seen in the experimental data (Figure 3a). These Rabi splittings are greater than a) the measured spectral width of the respective C=O ( $60 \text{ cm}^{-1}$ ),  $\text{CH}_2$  ( $30 \text{ cm}^{-1}$ ), and  $\text{CH}_3$  ( $30 \text{ cm}^{-1}$ ) vibrational modes respectively, and b) the width of the bare cavity mode—measured using an off-resonance cavity to be  $45 \text{ cm}^{-1}$ . These data thus indicate that our microcavity system is in the strong coupling regime.<sup>[47]</sup> The results from this coupled oscillator model are

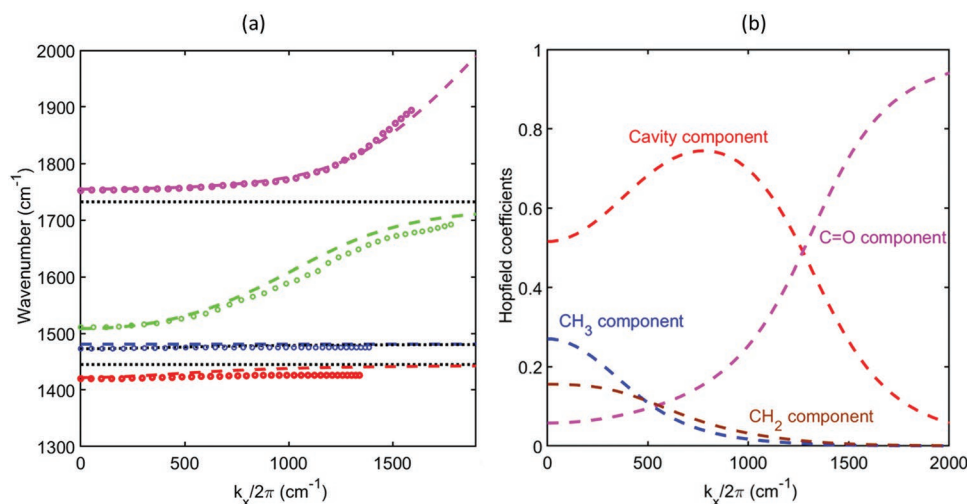


**Figure 4.** Coupled oscillator model for the planar cavity. a) Comparison between experimental (circles) and coupled oscillator model (dashed lines) for: the lower polariton (L) mode (red), the lower middle polariton (M1) mode (blue), the upper middle polariton (M2) mode (green), and the upper polariton (U) mode (magenta) for grating mode. The horizontal dotted lines in black show the energies of the C=O, CH<sub>2</sub>, and CH<sub>3</sub> vibrational modes, respectively. The bare cavity mode is shown as a brown dashed line. b) Hopfield coefficients of the upper middle polariton (M2). The contribution of the cavity mode is shown in red, the C=O mode in magenta, the CH<sub>2</sub> mode in brown, and the CH<sub>3</sub> mode in blue. The data shown were found by calculating the eigenvalues and eigenvectors of Equation (3).

shown in **Figure 4**, in Figure 4a experimental data (circles) are also shown corresponding to the maxima of the transmittance spectra shown in Figure 3a. In Figure 4a we also show the positions of the uncoupled (bare) microcavity, and the C=O, the CH<sub>2</sub>, the CH<sub>3</sub> resonances as dotted lines.

In addition to allowing extraction of the coupling strengths, the coupled oscillator model enables us to determine the contribution of the different resonances to each polariton band through the Hopfield coefficients. In particular we can use this approach to examine the contribution that the different vibrational modes make to the upper middle polariton (M2).

In Figure 4b we show the contribution of the cavity mode, the C=O mode, the CH<sub>2</sub> mode, CH<sub>3</sub> mode to the upper middle polariton band M2 as a function of in-plane wavevector. At in-plane wavevector  $\approx 530 \text{ cm}^{-1}$  we see that the M2 polariton has contributions of  $\approx 33\%$  from the C=O, CH<sub>2</sub>, and CH<sub>3</sub> modes (equal contributions of 11% from each), the remaining 67% being photonic (cavity mode) in character. These data show that the upper middle polariton involves hybridization of the three different vibrational resonances associated with the same molecular unit.

Microcavities are just one class of structure that produce confined light fields; here we also explored a second type of confined light field that associated with a surface plasmon.<sup>[48]</sup> We noted earlier that to couple to such modes with incident light requires some kind of momentum matching. In contrast with the attenuated total reflection technique employed by Memmi et al.<sup>[30]</sup> we made use of grating coupling, a technique previously used with great success by Vasa et al. to observe Rabi oscillations associated with excitonic strong coupling.<sup>[41]</sup> A schematic of the sample structure we used is shown in Figure 1b. The plasmonic surface is provided by a 100 nm gold film fabricated in the form of a grating using electron beam lithography. The grating period was 7.2  $\mu\text{m}$  with a 1  $\mu\text{m}$  gap on a CaF<sub>2</sub> substrate. This choice of period was made to enable coupling of

incident light to the surface plasmon mode on the Au/PMMA interface at a convenient angle of incidence. FTIR spectra for a range of incident angles were acquired; the results, in the form of a dispersion plot, are shown in **Figure 5a**.

As for the microcavity, we also calculated a dispersion plot using numerical modeling, shown in Figure 5b. There is broad agreement between the numerically modeled data and the experiment, some of the differences in detail might be attributed to variations in the grating across the  $\approx 2 \text{ mm}$  spot size used in the FTIR measurements.

Again, and as for the microcavity system, we also modeled the surface plasmon system using the four coupled oscillator model. Here the surface plasmon mode replaces the cavity mode as one of the oscillators, together with the three vibrational modes, C=O, CH<sub>2</sub>, and CH<sub>3</sub>. For the plasmon mode, we took the uncoupled dispersion from numerically modeled data (Figure S4, Supporting Information) in which the oscillators strengths were set to zero.

The best match between the eigenvalues obtained from this approach and those seen in the experimental data (Figure 5) was obtained with:  $\Omega_{\text{C=O}} = 75 \text{ cm}^{-1}$ ,  $\Omega_{\text{CH}_2} = 20 \text{ cm}^{-1}$ , and  $\Omega_{\text{CH}_3} = 35 \text{ cm}^{-1}$ . The resulting polariton frequencies are plotted as colored dashed lines in Figure 5a.

These splittings are approximately half of those obtained from the planar microcavity; the microcavity mode appears to offer a higher (average) electric field strength.<sup>[47]</sup> Again, these splittings need to be compared to: a) the measured spectral width of the respective C=O (60  $\text{cm}^{-1}$ ), CH<sub>2</sub> (30  $\text{cm}^{-1}$ ), and CH<sub>3</sub> (30  $\text{cm}^{-1}$ ) vibrational modes respectively, and b) the width of the bare cavity mode, 45  $\text{cm}^{-1}$ . We see that for the plasmon system only, the splitting associated with the C=O vibrational resonance fully satisfies the strong coupling condition.

In **Figure 6b**, we show the calculated Hopfield coefficients for the lower middle polariton in the plasmon system. We see that although the lower middle polariton does have some character

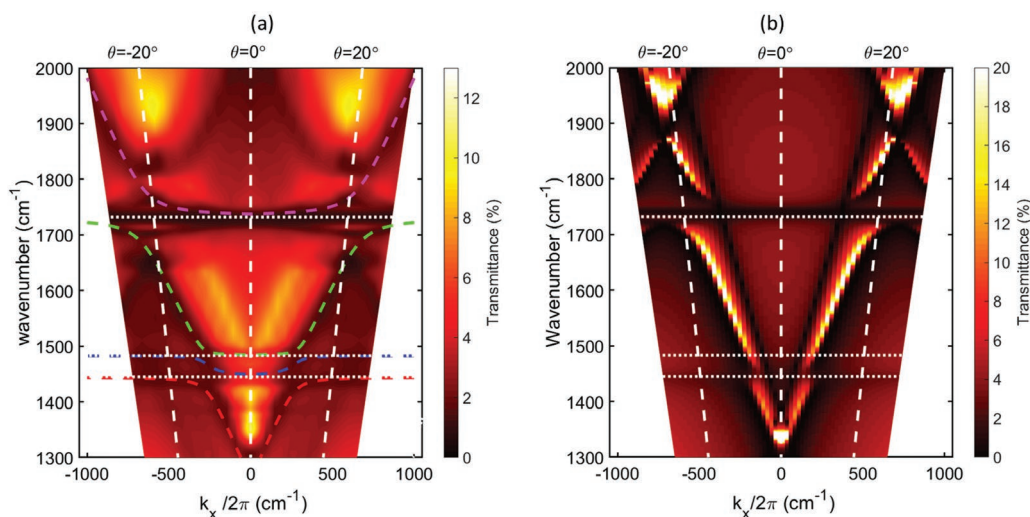


**Figure 5.** Dispersion plots for the plasmon system. a) Dispersion diagram derived from experimental data. Infrared transmittances of the plasmon sample shown in Figure 1b are shown as a function of frequency  $\text{cm}^{-1}$  and in-plane wavevector  $k_x$ . The horizontal white dotted lines indicate the energy of the C=O ( $\approx 1732 \text{ cm}^{-1}$ ),  $\text{CH}_2$  ( $\approx 1481 \text{ cm}^{-1}$ ), and  $\text{CH}_3$  ( $\approx 1445 \text{ cm}^{-1}$ ) vibrational resonances. The maximum polar angle for which these data were acquired was  $\Theta = 30^\circ$ . Angles of incidence equal to  $\pm 20^\circ$  are indicated as white dashed lines, and correspond to the angles at which anticrossing of the plasmon mode occurs with the C=O resonance. Also shown are the calculated positions (colored dashed lines) of the polariton branches from the coupled oscillator model: lower polariton (red), middle polariton (blue), and upper polariton (magenta). b) Numerically modeled data using COMSOL Multiphysics. Calculated transmittance is shown using a color scale, and plotted as a function of frequency  $\text{cm}^{-1}$  and in-plane wavevector  $k_x$ .

inherited from all three vibrational resonances, their contribution is relatively small, around 5% each. This lower contribution than for the cavity mode might also be attributed to the lower field strength of the plasmon mode as sampled by the PMMA film.

It is also clear that the match between the data and the model for the plasmon system (Figure 6a) is poorer than it was for the microcavity system (Figure 4a). Several factors may contribute to this: first, more than one diffracted plasmon mode contributes to the data shown in Figure 5a, for simplicity we only

included one of them; second, the dispersion of the plasmon mode depends sensitively on the profile of the grating,<sup>[49]</sup> for simplicity we have taken a simple rectangular profile here, and we have ignored any band distortions due to grating coupling of plasmon modes; third, determining the position of the plasmon using dispersion data from transmittance data can be problematic owing to the Fano-like character of the features involved. Despite these limitations, the coupled oscillator reproduces reasonably well the anticrossings seen in the experiment.

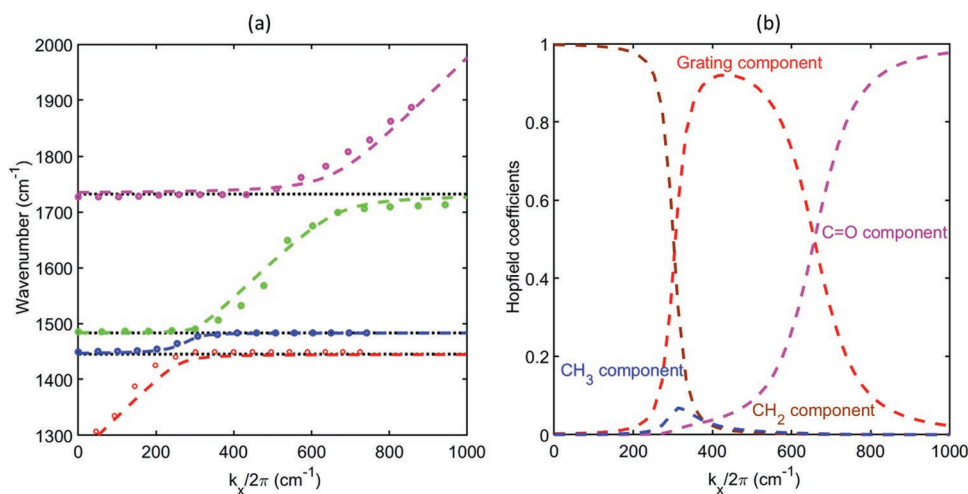


**Figure 6.** Coupled oscillator model for the plasmon system. a) Comparison between experimental data (circles) and the coupled oscillator model (dashed lines) for: the lower polariton (L) mode (red), the lower middle polariton (M1) mode (blue), the upper middle polariton (M2) mode (green), and the upper polariton (U) mode (magenta). The horizontal dotted lines (black) show the energies of the C=O,  $\text{CH}_2$ , and  $\text{CH}_3$  vibrational modes, respectively. The bare plasmon mode is shown as a brown dashed line. b) Hopfield coefficients of the upper middle polariton (M2). The contribution of the plasmon mode is shown in red, the  $\text{CH}_3$  mode in blue, the  $\text{CH}_2$  mode in brown, and the C=O mode in magenta. The data shown were found by calculating the eigenvalues and eigenvectors of Equation (3).

### 3. Conclusion

In summary, our results show that distinct molecular vibrational resonances, here associated with C=O, CH<sub>2</sub>, and CH<sub>3</sub>, may be hybridized by strong coupling each of them to the same cavity/plasmon mode. The extent to which the three vibrational resonances contribute to the upper middle polariton in the cavity system (11%) is comparable to that in the first report of hybridizing two excitonic resonances via strong coupling.<sup>[17]</sup> For the case of the plasmon mode we found that only the coupling with the C=O bond fully met the strong coupling criteria, and that the associated polariton, although involving all three molecular resonances, only did so to the extent of 5%. Nonetheless, it is clear that strong coupling can hybridize multiple different molecular resonances of a single molecular unit, and that consequently strong coupling offers an interesting means by which to control molecular systems.

Hybridized vibrational resonances may also be interesting in the context of vibrationally dressed states.<sup>[10,50]</sup> A challenge for the strong coupling community is to devise means by which the extent of possible hybridization can be increased. This might be achieved by employing confined light fields that exhibit greater field enhancement than the planar metal-clad cavity used here. Possible routes to accomplish this include planar cavities that use dielectric stacks rather than metal mirrors,<sup>[51]</sup> and localized resonances.<sup>[52]</sup> Care will be needed though since there is often a trade-off between field enhancement and cavity volume to consider.<sup>[53]</sup> An interesting alternative may be to explore a hierarchical approach that mixes plasmonic resonances and vibrational ones, much as was recently accomplished for exciton resonances by Bisht et al.<sup>[54]</sup>

### 4. Experimental Section

**Optical Microcavities:** The cavity mirrors were both made of gold by e-beam-assisted evaporation and each had a nominal thickness of 12 nm. The PMMA (molecular weight 950 K) was spin coated from a solution diluted in 11% anisole to achieve a layer thickness of 2.26 μm, as measured with a profilometer (see Figure S3, Supporting Information). The microcavity was formed on a silicon substrate that had a minimal oxide thickness layer.

**Grating Fabrication:** 1D grating structures were produced using electron beam lithography. Briefly, an e-beam resist (PMMA: 950 K A9) was spun (4000 rpm) onto a 20 mm square silicon wafer substrate to obtain a thickness of 400 nm. The substrate was then heated to 180 °C for 10 min to remove the solvent. For the electron beam lithography a 20 nA beam current was used to write the desired pattern. Following exposure the resist was developed (MEK+MIBK+IPA) for 40 s. A thin 100 nm gold film was then deposited by thermal evaporation, followed by a lift-off process to leave the desired gold stripe grating (see Figure 1b).

**Infrared Transmittance:** The infrared transmittance of the samples was measured using an FTIR spectrometer (Bruker V8). These data were normalized with respect to a transmittance spectrum acquired with no sample; background subtraction was also undertaken. To improve the signal-to-noise ratio, averaging over 128 scans was carried out.

**Numerical Modeling:** For the COMSOL calculations, the modeling volume comprising a 3 μm layer of silicon was overlain with a 12 nm gold thin film, covered by 2.26 μm layer of PMMA, another layer of 12 nm thin Au film to form a cavity, and finally followed by 3 μm of air layer. Periodic boundary conditions were added in the plane of the cavity. A minimum mesh element size of 0.22 nm was used, while the maximum mesh element size was 185 nm.

### Supporting Information

Supporting Information is available from the Wiley Online Library or from the author. The research data supporting this publication can be accessed at <https://doi.org/10.24378/exe.1403>.

### Acknowledgements

The authors acknowledge financial support from the Engineering and Physical Sciences Research Council (EPSRC) of the United Kingdom, via the EPSRC Centre for Doctoral Training in Metamaterials (Grant No. EP/L015331/1). W.L.B. acknowledges the support of the European Research Council through project Photmat (ERC-2016-AdG-742222: [www.photmat.eu](http://www.photmat.eu)). The authors also wish to thank Isaac Luxmoore, Stephen Lynch and Chris Hodges for assistance during the early stages of this work.

### Conflict of Interest

The authors declare no conflict of interest.

### Keywords

hybrid polaritons, optical microcavities, Rabi splitting, strong coupling, vibrational resonance

Received: March 6, 2019

Revised: June 3, 2019

Published online: June 19, 2019

- [1] D. G. Lidzey, D. D. C. Bradley, M. S. Skolnick, T. Virgili, S. Walker, D. M. Whittaker, *Nature* **1998**, 395, 53.
- [2] B. Barnes, F. García Vidal, J. Aizpurua, *ACS Photonics* **2018**, 5, 1.
- [3] A. Shalabney, J. George, J. Hutchison, G. Pupillo, C. Genet, T. W. Ebbesen, *Nat. Commun.* **2015**, 6, 5981.
- [4] T. W. Ebbesen, *Acc. Chem. Res.* **2016**, 49, 2403.
- [5] F. Herrera, F. C. Spano, *Phys. Rev. Lett.* **2016**, 116, 238301.
- [6] K. Bennett, M. Kowalewski, S. Mukamel, *Faraday Discuss.* **2016**, 194, 259.
- [7] J. Feist, J. Galego, F. J. Garcia-Vidal, *ACS Photonics* **2018**, 5, 205.
- [8] R. F. Ribeiro, L. A. Martínez-Martínez, M. Du, J. Campos-Gonzalez-Angulo, J. Yuen-Zhou, *Chem. Sci.* **2018**, 9, 6325.
- [9] J. A. Hutchison, T. Schwartz, C. Genet, E. Devaux, T. W. Ebbesen, *Angew. Chem., Int. Ed.* **2012**, 51, 1592.
- [10] J. Galego, F. J. Garcia-Vidal, *Phys. Rev. X* **2015**, 5, 041022.
- [11] T. Schwartz, J. A. Hutchison, C. Genet, T. W. Ebbesen, *Phys. Rev. Lett.* **2011**, 106, 196405.
- [12] J. Feist, F. J. Garcia-Vidal, *Phys. Rev. Lett.* **2015**, 114, 196402.
- [13] D. M. Coles, N. Somaschi, P. Michetti, C. Clark, P. G. Lagoudakis, P. G. Savvidis, D. G. Lidzey, *Nat. Mater.* **2014**, 13, 712.
- [14] X. Zhong, T. Chervy, S. Wang, J. George, A. Thomas, J. A. Hutchison, E. Devaux, C. Genet, T. W. Ebbesen, *Angew. Chem., Int. Ed.* **2016**, 55, 6202.
- [15] K. Georgiou, P. Michetti, L. Gai, M. Cavazzini, Z. Shen, D. G. Lidzey, *ACS Photonics* **2018**, 5, 258.
- [16] X. Zhong, T. Chervy, L. Zhang, A. Thomas, J. George, C. Genet, J. A. Hutchison, T. W. Ebbesen, *Angew. Chem., Int. Ed.* **2017**, 56, 9034.
- [17] D. G. Lidzey, D. D. C. Bradley, A. Armitage, S. Walker, M. S. Skolnick, *Science* **2000**, 288, 1620.
- [18] M. Sliotsky, X. Liu, V. M. Menon, S. R. Forrest, *Phys. Rev. Lett.* **2014**, 112, 076401.

- [19] S. Baieva, J. A. Ihalainen, J. J. Toppari, *J. Chem. Phys.* **2013**, *138*, 044707.
- [20] A. I. Väkeväinen, R. J. Moerland, H. T. Rekola, A.-P. Eskelinen, J.-P. Martikainen, D.-H. Kim, P. Törmä, *Nano Lett.* **2014**, *14*, 1721.
- [21] M. Muallem, A. Palatnik, G. D. Nessim, Y. R. Tischler, *J. Phys. Chem. Lett.* **2016**, *7*, 2002.
- [22] V. F. Crum, S. R. Casey, J. R. Sparks, *Phys. Chem. Chem. Phys.* **2018**, *20*, 850.
- [23] J. George, T. Chervy, A. Shalabney, E. Devaux, H. Hiura, C. Genet, T. W. Ebbesen, *Phys. Rev. Lett.* **2016**, *117*, 153601.
- [24] J. P. Long, B. S. Simpkins, *ACS Photonics* **2015**, *2*, 130.
- [25] A. Shalabney, J. George, J. A. Hutchison, G. Pupillo, C. Genet, T. W. Ebbesen, **2014**, *arXiv*: 1403.1050.
- [26] B. S. Simpkins, K. P. Fears, W. J. Dressick, B. T. Spann, A. D. Dunkelberger, J. C. Owrutsky, *ACS Photonics* **2015**, *2*, 1460.
- [27] R. M. A. Vergauwe, J. George, T. Chervy, J. A. Hutchison, A. Shalabney, V. Y. Torbeev, T. W. Ebbesen, *J. Phys. Chem. Lett.* **2016**, *7*, 4159.
- [28] M. Muallem, A. Palatnik, G. D. Nessim, Y. R. Tischler, *Ann. Phys. (Berlin)* **2016**, *528*, 313.
- [29] A. D. Dunkelberger, B. T. Spann, K. P. Fears, B. S. Simpkins, J. C. Owrutsky, *Nat. Commun.* **2016**, *7*, 13504.
- [30] H. Memmi, O. Benson, S. Sadofev, S. Kalusniak, *Phys. Rev. Lett.* **2017**, *118*, 126802.
- [31] W. Ahn, I. Vurgaftman, A. D. Dunkelberger, J. C. Owrutsky, B. S. Simpkins, *ACS Photonics* **2018**, *5*, 158.
- [32] T. Chervy, A. Thomas, E. Akiki, R. M. A. Vergauwe, A. Shalabney, J. George, E. Devaux, J. A. Hutchison, C. Genet, T. W. Ebbesen, *ACS Photonics* **2018**, *5*, 217.
- [33] S. R. Casey, J. R. Sparks, *J. Phys. Chem. C* **2016**, *120*, 28138.
- [34] J. George, A. Shalabney, J. A. Hutchison, C. Genet, T. W. Ebbesen, *J. Phys. Chem. Lett.* **2015**, *6*, 1027.
- [35] M. Hertzog, P. Rudquist, J. A. Hutchison, J. George, T. W. Ebbesen, K. Börjesson, *Chem. - Eur. J.* **2017**, *23*, 18166.
- [36] A. Thomas, J. George, A. Shalabney, M. Dryzhakov, S. J. Varma, J. Moran, T. Chervy, X. Zhong, E. Devaux, C. Genet, J. A. Hutchison, T. W. Ebbesen, *Angew. Chem., Int. Ed.* **2016**, *55*, 11462.
- [37] A. D. Dunkelberger, R. B. Davidson, W. Ahn, B. S. Simpkins, J. C. Owrutsky, *J. Phys. Chem. A* **2018**, *122*, 965.
- [38] B. Xiang, R. F. Ribeiro, A. D. Dunkelberger, J. Wang, Y. Li, B. S. Simpkins, J. C. Owrutsky, J. Yuen-Zhou, W. Xiong, *Proc. Natl. Acad. Sci. USA* **2018**, *115*, 4845.
- [39] K. E. Dorfman, S. Mukamel, *Proc. Natl. Acad. Sci. USA* **2018**, *115*, 1451.
- [40] J. Dintinger, S. Klein, F. Bustos, W. L. Barnes, T. W. Ebbesen, *Phys. Rev. B* **2005**, *71*, 035424.
- [41] P. Vasa, W. Wang, R. Pomraenke, M. Lammers, M. Maiuri, C. Manzoni, G. Cerullo, C. Lienau, *Nat. Photonics* **2013**, *7*, 128.
- [42] H. Nagai, *J. Appl. Polym. Sci.* **1963**, *7*, 1697.
- [43] I. J. Luxmoore, P. Q. Liu, P. Li, J. Faist, G. R. Nash, *ACS Photonics* **2016**, *3*, 936.
- [44] R. L. Olmon, B. Slovick, T. W. Johnson, D. Shelton, S.-H. Oh, G. D. Boreman, M. B. Raschke, *Phys. Rev. B* **2012**, *86*, 235147.
- [45] E. D. Palik, *Handbook of Optical Constants of Solids*, Academic Press, Orlando, Florida, USA **1998**.
- [46] I. H. Malitson, *Appl. Opt.* **1963**, *2*, 1103.
- [47] L. Tropic, M. C. Gather, *Adv. Opt. Mater.* **2018**, *6*, 1800203.
- [48] J. Bellessa, C. Bonnard, J. C. Plenet, J. Mugnier, *Phys. Rev. Lett.* **2004**, *93*, 036404.
- [49] W. L. Barnes, T. W. Preist, S. C. Kitson, J. R. Sambles, *Phys. Rev. B* **1996**, *54*, 6227.
- [50] F. Herrera, F. C. Spano, *ACS Photonics* **2018**, *5*, 65.
- [51] O. Kapon, R. Yitzhari, A. Palatnik, Y. R. Tischler, *J. Phys. Chem. C* **2017**, *121*, 18845.
- [52] W. Wan, X. Yang, J. Gao, *Opt. Express* **2016**, *24*, 12367.
- [53] R. Chikkaraddy, B. de Nijs, F. Benz, S. J. Barrow, O. A. Scherman, E. Rosta, A. Demetriadou, P. Fox, O. Hess, J. J. Baumberg, *Nature* **2016**, *535*, 127.
- [54] A. Bisht, J. Cuadra, M. Wersäll, A. Canales, T. J. Antosiewicz, T. Shegai, *Nano Lett.* **2019**, *19*, 189.